

A metallogenic model for the supergiant gold system in Jiaodong province: Constraints from crustal velocity structure

Jue HOU^{1,2,5}, Tao XU^{3,6*}, Yinshuang AI^{4,6}, Guiping YU⁷, Yingjie YANG⁸,
Bo XU⁹ & Qingfei WANG^{9†}

¹ Institute of Geophysics, China Earthquake Administration, Beijing 100081, China;

² State Key Laboratory of Lithospheric Evolution, Institute of Geology and Geophysics, Chinese Academy of Sciences, Beijing 100029, China;

³ Key Laboratory of Mineral Resources, Institute of Geology and Geophysics, Chinese Academy of Sciences, Beijing 100029, China;

⁴ Key Laboratory of Earth and Planetary Physics, Institute of Geology and Geophysics, Chinese Academy of Sciences, Beijing 100029, China;

⁵ University of Chinese Academy of Sciences, Beijing 100049, China;

⁶ Innovation Academy for Earth Science, Chinese Academy of Sciences, Beijing 100029, China;

⁷ College of Earth Science, Guilin University of Technology, Guilin 541004, China;

⁸ Department of Earth and Space Sciences, Southern University of Science and Technology, Shenzhen 518055, China;

⁹ State Key Laboratory of Geological Processes and Mineral Resources, China University of Geosciences, Beijing 100083, China

Received January 29, 2023; revised July 20, 2023; accepted August 22, 2023; published online November 3, 2023

Abstract We investigate the role of crustal architectures playing in controlling the genesis and nature of supergiant Jiaodong orogenic gold system via seismic imaging. We deployed an NWW-SEE-trending broadband seismic linear array traversing the province to construct a shear wave velocity (V_S) transect based on ambient noise tomography. Our crustal V_S transect reveals a prominent low velocity zone (LVZ) at 12–20 km depths across the whole province and high V_S anomalies at 8–12 km depths underneath the western part that hosts most of the ore tonnage. We interpret the former as a hydrothermal alteration zone related to mineralization and the latter as a crustal component containing large amounts of mafic rocks (e.g., amphibolites). In addition, a listric fault system and a strike-slip fault system are imaged in the western and eastern parts of the province, respectively. Combining features of crustal velocities with regional geological observations that ores are tempo-spatially associated with mafic dikes, we propose a model of gold metallogenic processes. In this model, ponding and degassing of the mafic magmas led to the formation of a hydrothermal alteration LVZ in the middle crust prior to mineralization. Later, auriferous fluid was released from this intra-crustal hydrothermal alteration zone as it was heated by upwelling asthenosphere. The ore fluid ascending along the listric fault system possibly leached extra gold from the upper-crustal amphibolites. Then, the gold-rich fluid migrated up along different fault systems, leading to the disseminated-veinlet mineralization with great gold endowment in the western listric fault system and the quartz-vein type mineralization with relatively small ore tonnage in the eastern strike-slip fault system.

Keywords Jiaodong gold province, Ore fluid, Ambient noise tomography, Crustal velocity structure

Citation: Hou J, Xu T, Ai Y, Yu G, Yang Y, Xu B, Wang Q. 2023. A metallogenic model for the supergiant gold system in Jiaodong province: Constraints from crustal velocity structure. *Science China Earth Sciences*, 66(12): 2898–2913, <https://doi.org/10.1007/s11430-023-1173-6>

1. Introduction

Crustal structures play crucial roles in the formation of large-

scale ore systems, including potential sources of fluids and metals, the migration networks for the fluids, and the traps of final ore deposition (e.g., Hou et al., 2015, 2021; Hoggard et al., 2020). The crustal controls on the porphyry-skarn ore systems have been well researched (e.g., Henley and Berger,

* Corresponding author (email: xutao@mail.iggcas.ac.cn)

† Corresponding author (email: wqf@cugb.edu.cn)

2013; Xu et al., 2021; Large et al., 2021), particularly in depicting intra-crustal causative magma migration system via geophysical methods (e.g., Yu et al., 2022). However, this kind of research has been rarely carried out for giant orogenic gold deposits which supply about 30% Au worldwide. This is because the orogenic gold system displays less traceable ore fluid sources and migration systems compared with porphyry-skarn ones.

The Jiaodong gold province, located in the southeastern margin of the North China Craton (NCC), is the largest gold producing base with an Au reserve greater than 5000 t, in China. A lot of studies on the Jiaodong gold deposits have been carried out before, and many important progresses, including mineralization timing, geological environment, and geodynamic setting, have been made (Fan et al., 2003; Yang et al., 2003a; Zhu et al., 2011, 2015; Song et al., 2015; Deng et al., 2020c, 2022, 2023). These studies suggest that the gold deposits were formed at ca. 120 Ma, the formation was mostly controlled by faults that developed in the Precambrian high-degree metamorphic basement and Mesozoic pre-ore granite plutons, with typical features of orogenic gold deposits despite the source of fluid being debated yet, and the deposits were generated in an extensional regime, associated with extensive emplacement of coeval mafic dike swarms, likely related to asthenosphere upwelling and craton destruction (e.g., Deng et al., 2014; Zhu et al., 2015; Deng and Wang, 2016).

However, the crucial factors for the massive Au mineralization in the province, especially their sources of fluids and metals, remain enigmatic. One view argues that the ore fluids were mainly derived from Neoproterozoic greenstones and associated Au mineralization was closely related to the metamorphism of the Precambrian greenstones, analogous to the “greenstone type” or “orogenic type” gold deposits in other ancient cratons worldwide (Groves et al., 1998; Goldfarb et al., 2001). The other view suggests that the ore fluids were sourced from Mesozoic granitic magmas that widely intruded the Precambrian metamorphic basement (Yang et al., 2003b; Cai et al., 2013; Ma et al., 2013; Tan et al., 2012). Nevertheless, both views have difficulties in explaining an important fact that the gold mineralization took place ca. 1800 Ma later than the release of metamorphic fluids during progressive metamorphism, and about 10 Ma postdated the gold-hosting granitoid plutons. It was also suggested that the fluid was most likely sourced from subducted Mesozoic oceanic crust and/or overlying sediment (Goldfarb et al., 2007; Goldfarb and Santosh, 2014), or from metasomatized mantle (Wang et al., 2020). However, how the mantle fluid migrated into the crustal level for tens of kilometers upward was still unclear. Although recent studies have proposed that the coeval mafic dike swarms sourced from metasomatized mantle could serve as a major supplier of the ore fluid (Wang et al., 2022), decimeter/centimeter-

wide mafic dikes are unlikely to provide sufficient fluids for the giant accumulation of gold. It should be pointed out that, among these three opinions mentioned above, the metals were regarded to share the same derivation as the ore fluids. Moreover, the amphibolites in the Jiaodong Group were also suggested to be a main metallic source, but the uncertainties of their distribution and volume in the Jiaodong crust hamper the evaluation of this possibility.

Another important issue is about the structural control on the Au ore system. Previous studies are mostly limited to individual deposits (Yang et al., 2018). The structural control in the terrane-scale is poorly understood. For example, three ore clusters have been recognized in the Jiaodong gold province (Figure 1). The western ore cluster is dominated by disseminated-veinlet mineralization with much great ore tonnage, whereas the central and eastern ore clusters are characterized by quartz-vein orebodies with much lesser ore tonnage. Although the reason for the differences in ore tonnage and mineralization style mentioned above is attributed to different ore-controlling structures in some studies (Deng et al., 2020c; Yu et al., 2020a), the specific structural ore-controlling role, especially the deep characteristics of ore-controlling structures, is currently unclear.

In the past two decades, a number of geophysical probes (Hou et al., 2022) on the lithospheric architecture in the Jiaodong Peninsula have been carried out, including seismic tomography to obtain 3D lithospheric V_p (Xu et al., 2002; Xu et al., 2009; Zhao et al., 2012; Su et al., 2016) and V_s (Li et al., 2018; Meng et al., 2019) velocity structures, 2D deep seismic sounding profiling (Ma et al., 1991; Jia et al., 2014; Pan et al., 2015), deep reflection seismic profiling (Yang, 2002), and receiver function imaging (Chen et al., 2006; Zheng et al., 2008). However, due to the limits posted by station distribution or imaging resolution, these geophysical studies were mainly focused on the major tectonic boundaries, with little attention paid to the fine structure of the crust. Recently, some geophysical fieldworks, including deploying a short-period dense array (Yu et al., 2020a, 2020b) and a reflection seismic profile (Yu et al., 2018), were carried out across the Jiaodong gold province to map the geometry of crustal faults and the lateral structure differences across the gold province. The seismic data from this dense seismic array provide a unprecedented opportunity to investigate the genetic link between the crustal structure and metallogenesis.

Thus, to image the fine crustal structure and explore its link with metallogenetic components (e.g., fluid source, metal derivation, fluid pathways and trap) in the Jiaodong gold province, we carry out ambient noise tomography (ANT) using the data recorded by the linear broadband seismic dense array supplemented by a few regional permanent stations (Figure 1). Combining the crustal structures constrained by ANT with geological observations, we propose a

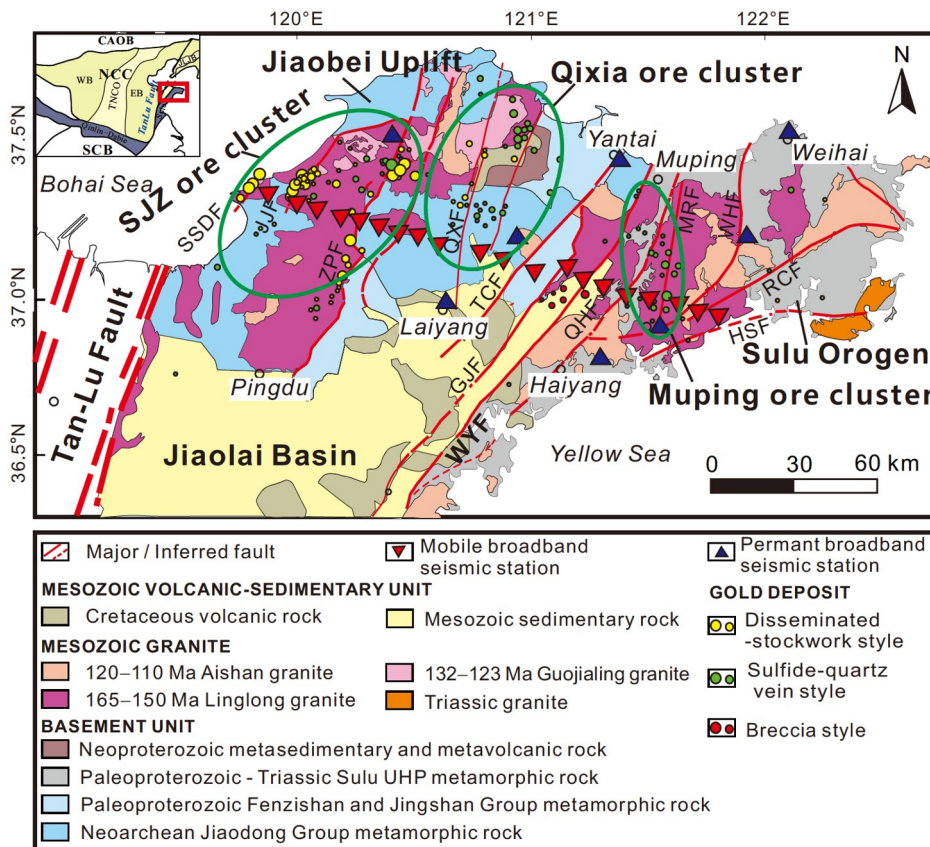


Figure 1 Geological map of the Jiaodong gold province (modified from Deng et al., 2020a). Temporary broadband seismic stations are denoted by red inverted triangles, and permanent broadband seismic stations are denoted by dark blue triangles. The SJZ, Qixia and Muping ore clusters are outlined by the three ellipses. JJF, Jiaojia fault; ZPF, Zhaoping fault; QXF, Qixia fault; TCF, Taocun fault; GJF, Guocheng-Jimo fault; WYF, Wulian-Yantai fault; QHF, Qingdao-Haiyang fault; MRF, Muping-Rushan fault; WHF, Weihai fault; RCF, Rongcheng fault; HSF, Haiyang-Shidao fault.

genetic model of the ore genesis involving fluid derivation, potential Au source, fault network, and structural control on ore system. It is of great significance for understanding the deep background of the massive enrichment of gold in the Jiaodong metallogenic province.

2. Geological background

The Jiaodong gold province, bounded by the Tan-Lu Fault to the west, is mainly composed of three tectonic units, namely the Jiaobei Uplift, Jiaolai Basin, and Sulu Orogen (Figure 1; Chough et al., 2000; Deng et al., 2020a). The Jiaobei Uplift and Jiaolai Basin constitute the Jiaobei Terrane, separated from the Sulu Orogen by the Wulian-Yantai Fault (WYF; Tang et al., 2008). The Jiaobei Uplift is dominantly composed of Precambrian high-grade metamorphic rocks, intruded by massive Mesozoic granites and mafic dike swarms (Figure 1; Deng et al., 2020b, 2020c). The Precambrian rocks mainly include tonalite-trondhjemite-granodiorite (TTG) gneiss, amphibolite of the Neoproterozoic Jiaodong Group, amphibolite- and greenschist-facies metasedimentary rocks of the Paleoproterozoic Fenzishan and Jingshan Groups, and metasedimentary rocks of the Meso-Neoproterozoic Penglai Group (Tang et al., 2008; Zhao et al., 2016). These Precambrian rocks experienced two major metamorphic events, taking place at ~2.5 Ga and ~1.8–1.9 Ga, respectively (Ames et al., 1996; Tang et al., 2008; Tam et al., 2011; Wan et al., 2011). The protoliths of amphibolites of the Jiaodong Group are tholeiitic basalts, generated in a subduction environment at ~2.5 Ga (Shan et al., 2015). The Sulu Orogen, formed by the collision between the NCC and Yangtze Block in Triassic, is mainly composed of Neoproterozoic granitic gneisses, coesite-bearing eclogite, quartzite and schist, which were intruded by Triassic granites (Huang et al., 2006; Zhang et al., 2012; Liu et al., 2018). The Jiaolai Basin mainly consists of Cretaceous fluvial, deltaic, and lacustrine sedimentary rocks, interbedded with volcanoclastic rocks, intermediate-silicic volcanic and volcanoclastic rocks, and basaltic rocks (Wang et al., 2016; Zhao et al., 2018).

Mesozoic granitoids are distributed widely in the Jiaodong Peninsula (Figure 1). The early Mesozoic granitoids (225–205 Ma) were emplaced at the eastern margins of the province (Figure 1; Guo et al., 2005). The late Mesozoic granitic rocks include biotite granite and muscovite granite

(165–150 Ma; Hou et al., 2007; Yang et al., 2012), granodiorite (132–123 Ma; Zhao et al., 2018), and monzogranite (120–110 Ma; Goss et al., 2010). Moreover, the mantle-derived mafic dikes were emplaced at 135–115 Ma throughout the province (Liu et al., 2009; Cai et al., 2013; Deng et al., 2017; Liang et al., 2018), from which some dikes intruded at 120 Ma show geochemical affinity with OIB, likely related to slab roll-back and associated asthenosphere upwelling (Deng et al., 2020a). The Jiaodong province has undergone tectonic erosion as a consequence of the lithosphere thinning since the late Jurassic, with two main phases of uplift in the Late Cretaceous and Paleogene (Zhu et al., 2011; Zhao et al., 2018).

The Jiaodong gold province can be divided into three main Au ore clusters, and the two clusters of Sanshandao-Jiaojia-Zhaoping (SJZ) and Qixia developed in the Jiaobei Uplift, and the third one of Muping in the Sulu Orogen (Figure 1). The regional gold deposits were controlled by a series of NNE- to NE-trending faults cutting the Precambrian basement and Mesozoic granite intrusions (Figure 1a; Deng et al., 2020a; Yang et al., 2014, 2018). These faults include the Sanshandao, Jiaojia, and Zhaoping faults in the SJZ ore cluster, the Qixia and Taocun faults in the Qixia ore cluster, and the Wulian-Yantai fault with subsidiary ones (e.g., Qingdao-Haiyang and Muping) in the Muping ore cluster (Figure 1). Studies indicate that the crustal extension and ductile deformation along the Zhaoping and Taocun faults occurred during 130–115 Ma, coeval to regional gold mineralization (Charles et al., 2013; Meng and Lin, 2021). The Zhaoping ductile zone was linked with a metamorphic core complex (Charles et al., 2013; Lin and Wei, 2018). Seismic data show that the Sanshandao, Jiaojia, Zhaoping and Qixia faults in the Jiaobei Uplift are mostly listric and vertically connected to lithosphere-scale structures at mid- to lower-crust levels (Song et al., 2015; Yu et al., 2018; Wang et al., 2022). The Wulian-Yantai fault, a boundary fault system, underwent a large-scale sinistral strike-slip movement in the Late Jurassic, an extension movement in the Early Cretaceous, and a small-scale dextral strike-slip movement in the Late Cretaceous (Zhang et al., 2007).

Two major styles of mineralization have been recognized in the Jiaodong gold province, i.e., a disseminated-stockwork style and a quartz-vein one. The ores of the former style are predominant in the SJZ ore cluster, whereas the quartz-vein ores dominated in the Muping ore cluster (Deng et al., 2020a). The ores of the former style, accounting for 80% of the total Au reserve in the province, are mainly hosted in cataclastic zones with pervasive K-feldspar, sericite and quartz alterations, suggesting intensive water-rock reaction during the Au mineralization. The latter style has relatively small ore tonnage and is restricted chiefly to subsidiary brittle faults with a narrow alteration halo, indicating a fluid

filling process. In addition, in terms of mineralization style and the order of ore-controlling faults, disseminated-stockwork mineralization is mainly developed in the primary ore-controlling faults (such as Sanshandao, Jiaojia, Zhaoping), while quartz-vein mineralization is mainly developed in subsidiary faults (Figure 1). Available dating data indicate that regardless of the type of mineralization, mineralization ages in the Jiaodong gold province are concentrated at ca. 120 Ma (Deng et al., 2020b; Zhang et al., 2020), demonstrating that they were formed in the same gold mineralization system.

3. Data and method

3.1 Seismic noise data

From September 2017 to September 2018, we deployed an NWW-SEE trending broadband linear seismic array across SJZ, Qixia and Muping ore clusters in the Jiaodong Peninsula (Figure 1, red inverted triangles). The array spans two clusters of SJZ and Muping. It is comprised of 20 stations with a total length of about 170 km, recording about one year of continuous three component seismic data. The data sampling rate is 40 Hz. In addition, we also collect continuous seismic data recorded at 8 adjacent broadband permanent stations (Figure 1, blue triangles) during the deployment duration to improve path coverage.

3.2 Data preprocessing

We obtain Rayleigh waves from cross-correlations of vertical components of seismic noise data. Before performing cross-correlation, we first preprocess continuous noise data recorded at individual stations, including cutting continuous data into a series of daily segments, decimating the sampling rate of noise data to 10 Hz, removing instrument response, mean and trend from them, and band-pass filtering all the waveforms at a 0.5–30 s period band. Then, we normalize the filtered waveforms using a running-absolute-mean normalization in the time domain and whiten the amplitude spectrum in the frequency domain (Bensen et al., 2007). After the preprocessing, we compute the cross-correlation functions (CCFs) of vertical components of daily data between any station pairs. Then, we obtain the final CCFs by linearly stacking all daily CCFs for each station pair. To further improve the signal-to-noise ratio of CCFs, we stack the positive and negative lags of CCFs to have the so-called symmetric components for subsequent measurements of dispersion curves.

Figure 2 shows the CCFs between all station pairs filtered at two period bands of 1–25 and 5–15 s, which displays clear Rayleigh wave signals. It is worth noting that there are some clear signals near zero lag time at the 5–15 s period band. As

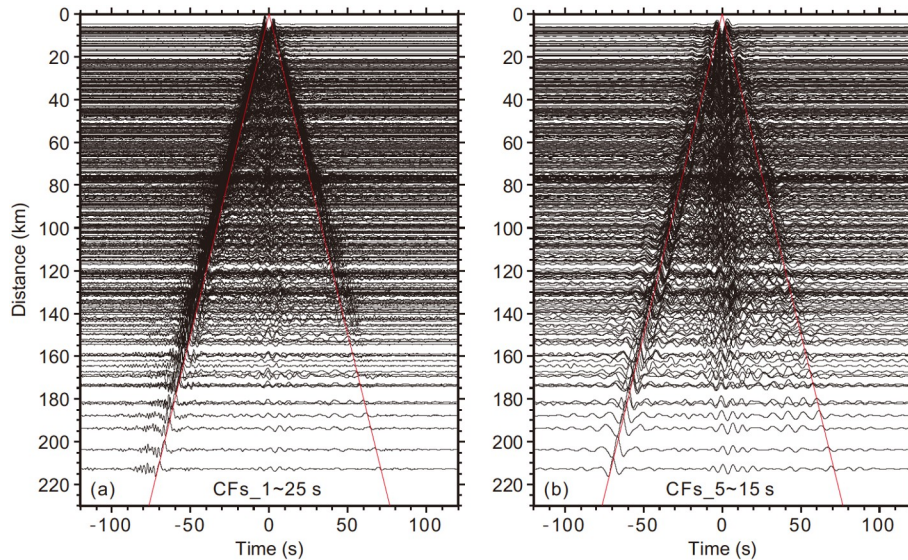


Figure 2 Cross-correlation functions of vertical components between the seismic stations. These cross-correlation functions are bandpass filtered at 1–25 and 5–15 s. The red line indicates that the speed of the wave train is 3 km/s.

the signals of near zero lag time on the CCFs only affect surface waves for station pairs with an interstation distance in the range of 30–50 km (Figure 2), we thus only measure dispersion curves from CCFs with interstation distances longer than 50 km to avoid the contamination of the near zero signals on the measurements of surface wave dispersion curves.

3.3 Measurements of dispersion curves

We adopt the image transformation technique developed by Yao et al. (2006) to measure phase velocity dispersion curves. We only select those CCFs with separations longer than two wavelengths (Yang et al., 2007; Yao et al., 2011; Luo et al., 2015) and with signal-to-noise ratios of surface waves larger than 5 for measurements. Limited by the station spacing and the spreading of our array, we measure phase velocity dispersion curves only at a period range of 1–20 s. Finally, we obtain 376 high quality Rayleigh wave phase velocity dispersion curves (Figure 3a), whose average values slowly change from 2.8 km/s at 1 s to 3.5 km/s at 20 s. As shown in Figure 3b, the number of ray paths at 3.5 s is the largest with a total of 234, while that at 20 s is the least with a total of 16. The characteristics of the average dispersion curve in Jiaodong peninsula are very close to the characteristics of the average dispersion curve obtained from previous studies in the adjacent area (the middle section of the Tanlu fault zone) (Luo et al., 2022), indicating the reliability of the data of this study. It should be noted that there are some local jitters in the dispersion curves in the 5–10 s period range, which are related to factors such as the signals of near zero lag time and the relatively low signal-to-noise ratio in this period range.

3.4 Phase velocity profile

The dispersion curves between station pairs are the average responses to the medium velocity along the path. Here, a generalized inversion method based on continuous model space is utilized (Tarantola and Valette, 1982; Montagner and Nataf, 1986; Yao et al., 2010) to invert for local dispersion curves at individual stations. In the inversion process, dispersion data with misfits greater than twice deviations are discarded automatically. The correlation lengths (red solid line in Figure 3b) are key parameters to balance the resolution and the stability of inversion. In this paper, they are determined by considering the wavelengths of different periods, the signal-to-noise ratio of data, the results of the checkerboard test and the scale of regional geological problems. We parameterize our inversion domain with a grid of $0.1^\circ \times 0.1^\circ$ nodes.

We first perform phase velocity tomography for each period from 1 to 20 s, and then assemble local phase velocity dispersion curves from the resulting phase velocity maps for each station along the linear seismic array as indicated in Figure 1, which is the profile of the temporary dense seismic array. These local dispersion curves along the profile are plotted as a 2D phase velocity profile in Figure 4.

3.5 S-wave velocity structure inversion

The local phase velocity dispersion curves at each grid point are reflections of underlying velocity structures beneath individual grid points. We adopt the iterative damped least square inversion method developed by Herrmann and Ammon (2002) to invert the local path dispersion curves for V_S structures based on CPS330 program package (Herrmann,

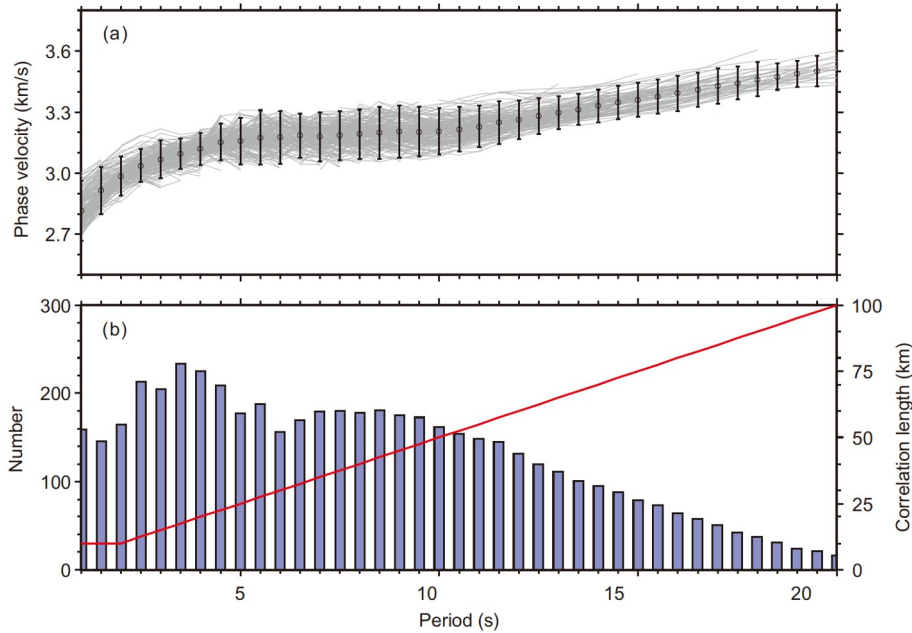


Figure 3 (a) Phase velocity dispersion curves. The black circles and error bars represent the average phase velocities of all the dispersion curves and their double standard deviations. (b) The histogram represents the number of phase velocity measurements retained for tomography at each period. The red line represents the correlation length used in tomography.

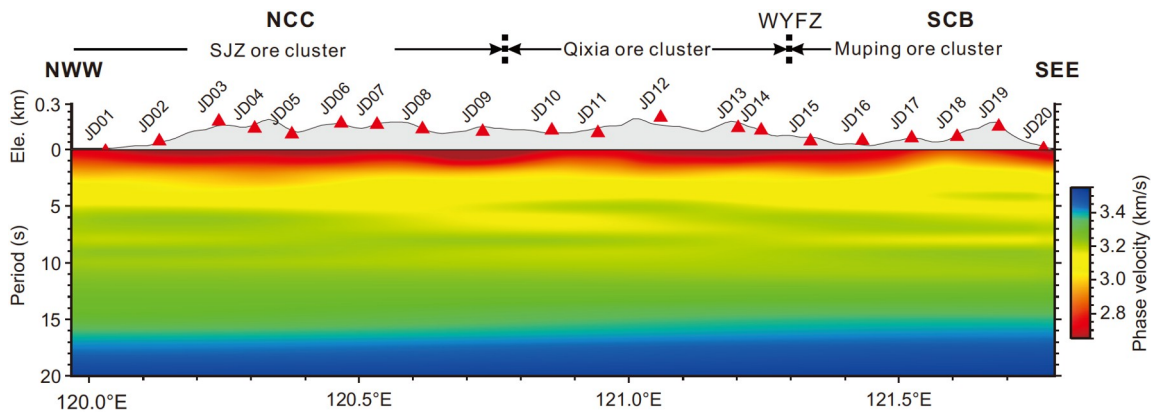


Figure 4 Phase velocity profile. NCC, North China Craton; SCB, South China Block; WYFZ, Wulian-Yantai fault zone; Ele., Elevation.

2013). As the phase velocities of Rayleigh wave are more sensitive to V_S than to V_P and density, V_P and density are scaled according to V_S and V_P/V_S ratio. The V_P/V_S ratio is fixed to 1.76 in the inversion, and the density is updated according to the Nafe-Drake relation (Ludwig et al., 1970; Brocher, 2005).

In the inversion process, the crust is divided into a series of 0.5 km thick layers. For a Poisson medium with a uniform half space, V_S at the depth of 1/3 wavelength of Rayleigh wave is about 1.1 times of the phase velocity (Shearer, 2009; Fang et al., 2015). Following this relationship, we construct an initial velocity model by converting the local dispersion curves (gray dotted line in Figure 5) to V_S . It should be noted that the initial velocity model at 0–20 km depth is estimated based on the average dispersion curve, whereas that at

20–33 km depth is determined by the linear transition by referring to the regional average crustal thickness (Pan et al., 2015; Yu et al., 2020b), and the velocity of the uppermost mantle is 4.3 km/s.

4. Results

4.1 Crustal V_S structure

The resulting V_S transect along the profile of our seismic array is plotted in Figure 6a. At the same time, to highlight the lateral and vertical variation characteristics of V_S structure, we calculate V_S perturbation (Figure 6b) and the vertical V_S gradient (Figure 6c). The V_S perturbation is defined as the deviation of V_S beneath each grid point relative to the aver-

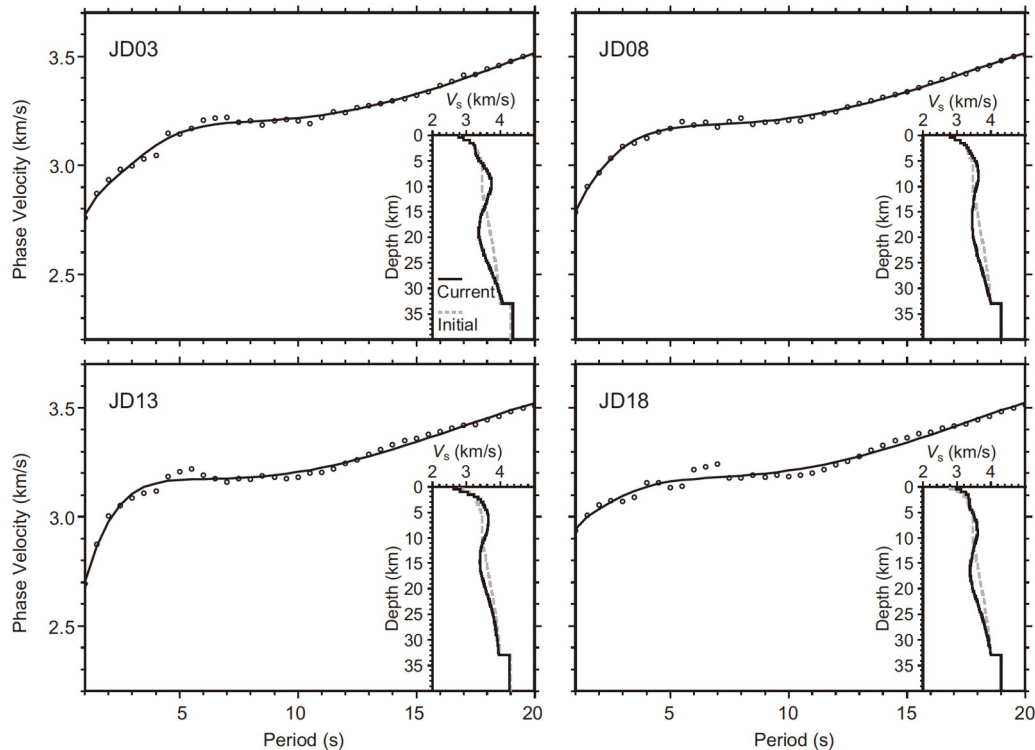


Figure 5 Examples of V_S inversions at four stations. At each panel, the black circles denote the observed dispersion curves, and the black solid lines represent the synthetic dispersion curves calculated based on the inverted results of V_S profiles. In the insets, the gray dotted line represents the initial velocity model, and the black solid line represents the inversion result.

age V_S of the same depth. Since only the dispersion data in the period band of 1–20 s are used in the inversion, which has weak sensitivities to structures at depths below 25 km, we thus mainly discuss the crustal structure above 25 km.

In our resulting V_S model, a low velocity zone (LVZ) is imaged in the middle crust with an average V_S of about 3.4 km/s. The lowest velocity within the LVZ appears beneath the Jiaobei Uplift; and the shallowest depth of the LVZ is underneath the Qixia ore cluster. There are two discontinuous high velocity bodies at the depth of 8–12 km: one beneath the SJZ ore cluster and the other beneath the east of the Qixia cluster. The V_S perturbations (Figure 6b) further highlight the lateral variations of V_S structure. The lateral transition position between the high and low velocity anomalies in the upper crust corresponds well with the main fault transition zones (Figure 6b), such as the Zhaoping, Qixia, and Wulian-Yantai fault zones.

Further analysis of the vertical velocity gradient (Figure 6c) is carried out to trace the top and bottom interfaces of the LVZ. The top interface of the LVZ is estimated to be ~10–13 km by tracing the maximum value of the negative gradient. And, the depth range of the bottom, which is defined by the appearance of positive velocity gradients, is ~16–21 km.

In addition, the velocity perturbation image (Figure 6b) shows that there are obvious structural differences among the

three ore clusters. The Qixia cluster and the Muping cluster are bounded by the Wulian-Yantai fault zone, and the velocity perturbations on both sides of the fault zone are characterized by significant lateral segmentation, whereas the transition between SJZ and Qixia ore clusters is relatively smooth, and the upper and middle crust at its junction presents a banded velocity anomaly with SE tendency, which is consistent well with the location of Zhaoping fault zone exposed on the surface.

4.2 Resolution analysis

This tomographic image we construct in this study is based on data from the linear temporary seismic array supplemented by a small number of regional permanent stations, and therefore the areas with good resolution are limited to the areas covered by the linear array. However, considering that our seismic array is nearly perpendicular to the strikes (NE–NNE) of the main structural lines, the influences of velocity heterogeneities outside the main linear array on the imaged velocity structure should be small. Therefore, we believe that the velocity structure beneath the survey line is well constrained by our inversion. To analyze the lateral resolution of the imaging results, we carry out a checkerboard test with the anomaly size set to be $0.4^\circ \times 0.4^\circ$ as shown in Figure 7a and 7e. In addition to the standard checkerboard test, we test

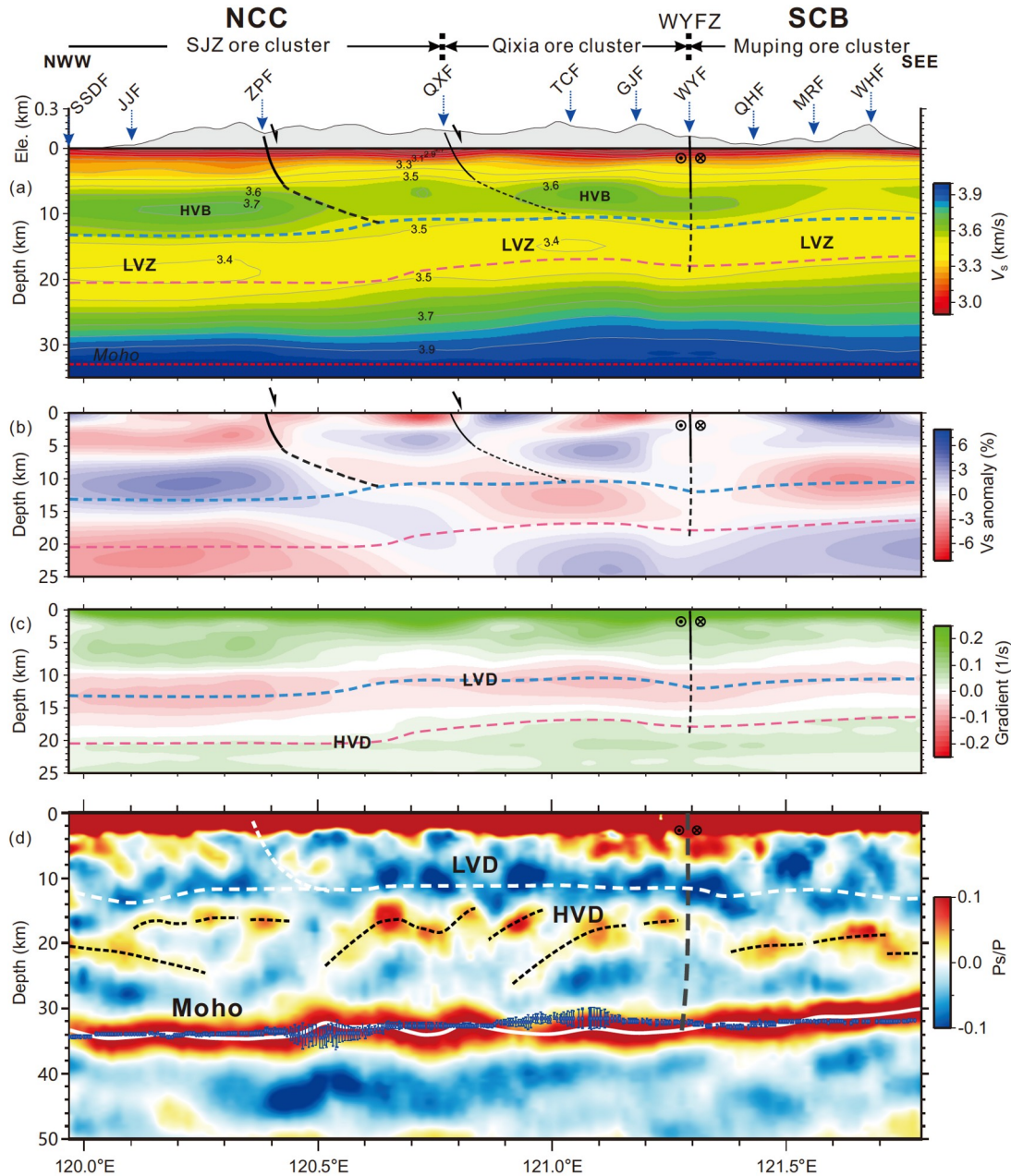


Figure 6 S-wave velocity transects plotted as (a) the absolute velocities, (b) velocity perturbations relative the average values at each depth, and (c) the vertical velocity gradients, respectively. In (a)–(c), black solid line represents the main fault observed on the surface; the black dotted line represents the inferred fault in the depths; the arrow represents the movement direction of the detachment fault; the blue dotted line and the red dotted line represent the top interface and the bottom interface of the low velocity layer, respectively. (d) CCP image of teleseismic P-wave receiver functions modified from Yu et al. (2020b). SSDF, Sanshandao fault; JJF, Jiaojia fault; ZPF, Zhaoping fault; QXF, Qixia fault; TCF, Taocun fault; GJF, Guocheng-Jimo fault; WYF, Wulian-Yantai fault; QHF, Qingdao-Haiyang fault; MRF, Muping-Rushan fault; WHF, Weihai fault; LVZ, low velocity zone; HVB, high velocity body; LVD, low velocity discontinuity; HVD, high velocity discontinuity.

banded models as shown in Figure 7f–7h for 2, 7 and 13 s dispersion data, respectively. The strikes of banded anomalies are nearly parallel to the strikes of main tectonic traces. The anomaly amplitude is set to $\pm 5\%$ and the inversion parameters are the same as the inversion for the field data.

The resolution test results show that the phase velocity inversions of 2, 7 and 13 s (Figure 7e–7h) have good lateral resolutions for banded anomalies with a size of 0.28° , 0.42°

and 0.64° . However, we also notice that, for the checkerboard test, only the velocity anomalies along the linear array are well resolved, and the anomalies off the linear array is not well resolved, which is expected given the uneven distribution of seismic stations we use in the inversion. As we are mainly interested in V_S transects along the seismic array, the relatively poor resolution in areas off the linear array does not affect our interpretation.

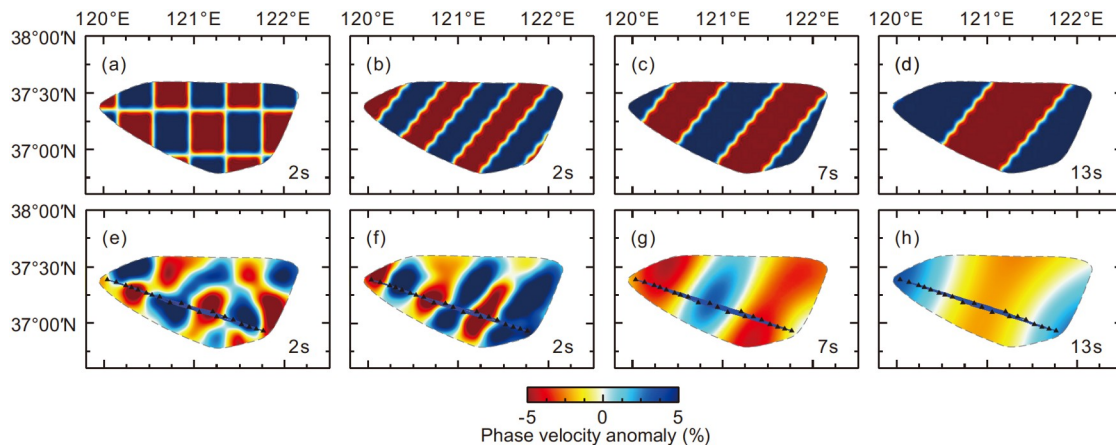


Figure 7 Resolution tests for phase velocity inversions. (a)–(d) The input models of phase velocities for four resolution tests, in which (a) is a standard checkerboard model with an anomaly size of $0.4^\circ \times 0.4^\circ$, (b)–(d) are three strip-shaped models with anomaly widths of 0.28° , 0.42° and 0.64° , respectively. The average phase velocities at 2, 7 and 13 s periods are 2.99, 3.18 and 3.30 km/s, respectively. (e)–(h) The inversion results of the resolution tests corresponding to the input models plotted in (a)–(d).

The vertical resolution of surface wave inversion is related to the periods of surface waves. Figure 8b shows Rayleigh wave phase velocity sensitivity kernels of different periods calculated based on the average V_s (Figure 8a, solid blue line) after the inversion. The longest period of phase velocity used in this paper is 20 s. The sensitivity kernel of 20 s shows that it is mostly sensitive to the crustal structure at ~ 20 km depth, and the resolution below 20 km gradually decreases with increasing depths. Therefore, the selection of an initial velocity model (especially below 20 km) may affect the inversion results. To better select a proper initial model and evaluate the effects of the initial model on inversion results, we take the dispersion data of station JD08 as an example to test different velocity models.

To analyze the differences in inversion results when the crustal velocity systematically deviates from a true model, we design four models, named M1, M2, M3 and M4 respectively, as shown in Figure 9a. M1 is the initial model used in this work. The velocity of M2 at the surface and the bottom of the crust is the same as that of M1, but the velocities in the domain change linearly with depth. Velocities of M3 and M4 are either systematically lower or higher than those of M2 at all depths. The V_p/V_s ratio, Moho depth, and mantle velocity for the four models are the same. The test results (Figure 9b) show that the initial velocity of the crust has little influence on the inversion results at depths above 27 km, validating the rationale that we only interpret V_s structures at depths above 25 km.

5. Discussion

5.1 Possible causes of abnormal crustal velocity structure

Our image results show that a LVZ in the middle crust is

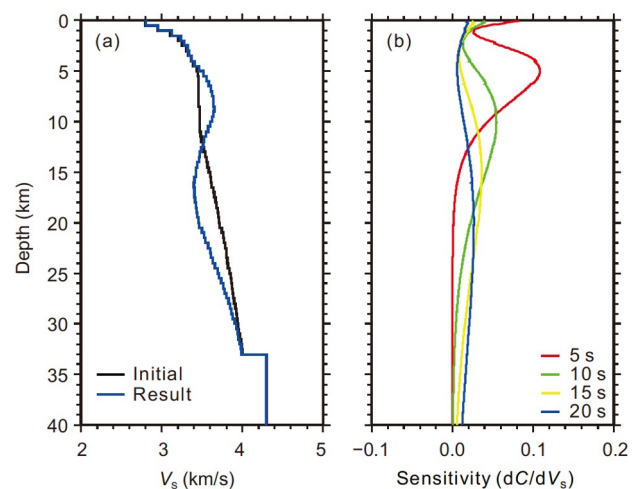


Figure 8 Average velocity profiles and sensitive kernel function. (a) The initial velocity model (black solid line) and the average velocity model (blue solid line) of the inversion results of all dispersion curves. (b) Phase velocity sensitivity kernels of Rayleigh waves at 5, 10, 15 and 20 s, which are calculated based on the average velocity model (blue solid line) plotted in the left panel.

universally developed in the Jiaodong province, consistent with previous seismic results (Zheng et al., 2008; Jia et al., 2014; Pan et al., 2015; Meng et al., 2019; Yu et al., 2020b; Luo et al., 2022). The bottom interface of this LVZ is coincident with the high velocity discontinuities (HVD) identified at about 16–20 km in the common conversion point stacking image of P-wave receiver functions (Figure 6; Yu et al., 2020b). In principle, such an intra-crustal LVZ can be attributed to three possibilities: a partial melting zone, a brittle-ductile transition zone, or an alteration zone (Kozlovsky, 1986; Marquis and Hyndman, 1992; Hacker et al., 2014; Diaferia and Cammarano, 2017; Flinders et al., 2018). Geological observations indicate that the Jiaodong gold province have witnessed an 8-km accumulative erosion since

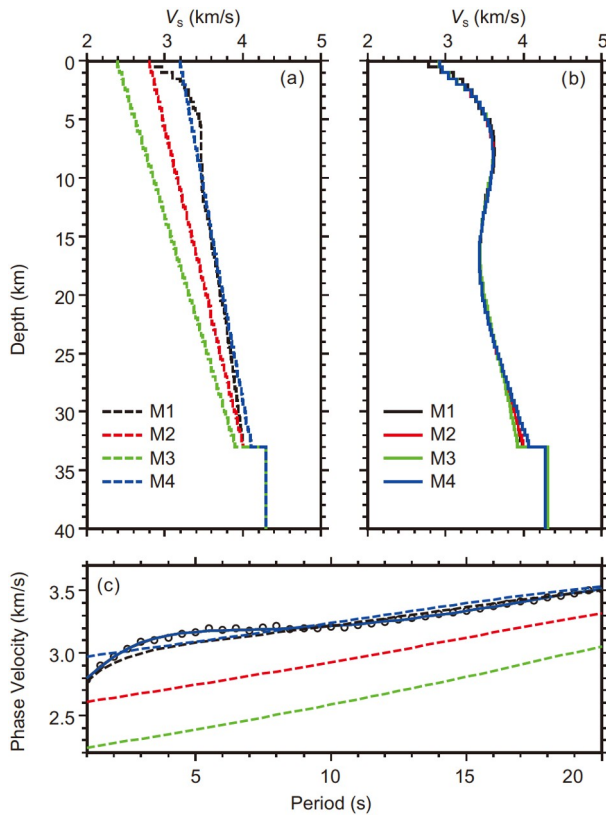


Figure 9 Tests of V_s inversions based on different initial models using the dispersion curves at station JD08. (a) Initial models with different crustal velocity structures, in which M1 is the initial model used in this paper, and M2, M3 and M4 are the linear models with different velocity gradients. (b) The inverted V_s profiles plotted using the same colors as those of the initial models from which the inverted V_s are obtained. (c) Fittings of the calculated dispersion curves to the observed ones (dots). The color and line-type of the calculated dispersion curves are consistent with those of corresponding initial models and inversion results.

the late Cretaceous, with the most intensive crustal extension occurring at 140–120 Ma (Zhao et al., 2018). Therefore, the HVD, regarded to mark the detachment zones (Yu et al., 2020b), should form at 140–120 Ma. This means that the LVZ in Jiaodong with a bottom depth of about 16–20 km at present should be originally located at 24–28 km depth considering the crustal erosion. This depth range is far beyond the low limit of the brittle-ductile transition depth (about 18 km; Sleep and Blanpied, 1994). Therefore, the LVZ in Jiaodong is unlikely to be the record of brittle-ductile transition zone.

Partial melting of the crust can lead to the development of large-scale LVZs, which has been confirmed by observations in the Tibetan Plateau. Large-scale LVZs are observed in the middle crust of Tibetan Plateau with the minimum V_s ranging between 2.9 and 3.3 km/s (Yang et al., 2012; Hacker et al., 2014), which are interpreted as the presence of partial melt. However, the V_s of the LVZ in Jiaodong is mainly between 3.4 and 3.5 km/s, and the lowest value is between 3.3 and 3.4 km/s, higher than that beneath Tibet and only slightly lower than that of the average middle crustal velocity

of the global continents (~ 3.6 km/s; Diaferia and Cammarano, 2017). Although this LVZ corresponds well with the high conductive layer of the middle crust in Jiaodong (Zhang et al., 2018), its absolute resistivity value and the surface heat flow value are comparable to the average values of the global continents (Martyn, 2003) and Chinese mainland (Jiang et al., 2019). Therefore, we argue that the presence of partial melt is also an unlikely candidate for the origin of the LVZ in Jiaodong.

Excluding the above two possibilities, it seems reasonable to interpret the middle crustal LVZ in Jiaodong as caused by hydrothermal alteration. Indeed, the low velocity characteristics of hydrothermal alteration zones are expected because altered rocks are a product of water-rock reaction and the density of altered rocks is relatively low if compared with unaltered rocks. Additionally, a water-rich layer (resembling a partial melt layer) can also generate a low velocity anomaly zone, but we believe that the LVZ cannot be the result of the liquid fluid layer at present. There are two reasons for this. Firstly, if it was the currently-present fluid rich layer, its low V_s anomalies would be very significant. However, as mentioned earlier, the low velocity anomalies observed in the LVZ are not the case. Secondly, the LVZ detected in Jiaodong is in the middle crust (16–20 km). Even along the fracture zone, the current groundwater is difficult to penetrate to this depth. Therefore, we believe that the LVZ is most likely the fossil fluid layer, namely the alteration zone. It should be pointed out that this LVZ, namely the alteration zone within the crust of Jiaodong gold province, is likely developed along the weak discontinuity within the crust.

Our V_s structure image shows that there are two discontinuous plate-like high-velocity bodies at 8–12 km depth in the upper crust: one beneath the SJZ and the other beneath the Xixia ore clusters (Figure 6a). Such high-velocity bodies are commonly interpreted as a crustal component with more Fe-Mg minerals (Christensen and Mooney, 1995). In the Jiaodong Peninsula, the Archean Jiaodong Group exposed at the surface constitutes the majority of the upper crust (Zhang et al., 2018), and its mafic rocks are dominantly composed of the Precambrian amphibolites. Therefore, we interpret the high-velocity bodies as a crustal component with large amounts of amphibolites.

The V_s perturbation image (Figure 6b) shows a SE-dipping velocity boundary between high velocities in the northwest and the low velocities in the southeast beneath the SJZ, roughly corresponding with the Zhaoping fault. Based on the extension trend of this velocity boundary and the main feature of the Zhaoping fault on the surface, which is a normal fault dipping eastward at a moderate angle (Deng et al., 2020a), we speculate that the Zhaoping fault is listric in shape and connected downward with the intra-crustal LVZ. A velocity boundary with low velocities in the northwest and high velocities in the southeast is also observed beneath the

Qixia ore cluster, corresponding with the Qixia fault (Figure 6b). The shape of this velocity boundary is similar to the one beneath the Zhaoping fault, suggesting the Qixia fault is probably listric in shape and connected to the underlying LVZ. Moreover, we observe a velocity discontinuity beneath the conjunction between Qixia and Muping ore clusters (Figure 6b), corresponding well with the Wulian-Yantai and Muping faults on the surface. The image suggests that the Wulian-Yantai fault is nearly vertically dipping and cuts through the upper and middle crust, exhibiting typical strike-slip fault occurrence characteristics, which is consistent with the high angle sinistral strike-slip feature on the surface of the Wulian-Yantai fault (Yu et al., 2020b).

5.2 Implications for Jiaodong gold mineralization

The V_S profile reveals that the crustal architecture in Jiaodong is characterized by a middle-crust alteration zone and an overlying amphibolite-rich upper crust. The integrated analysis presented below suggests that crustal structure not only served as a transport pipeline network for gold ore-forming fluids, but also controlled the mineralization style of gold deposits. At the same time, the crust itself also served as an additional Au source in the Jiaodong mineralization system.

5.2.1 Source and migration network of fluids in gold mineralization system

The source of ore-forming fluids in the mineralization system of Jiaodong gold province is still a mystery and has been a controversial issue. Although, solely based on our crustal V_S structure, it is difficult to determine the direct source, our V_S structure can reveal the transport network of fluids within the crust. Due to strong water-rock reactions and other alteration processes that occur during fluid migration, it will result in an LVZ. The LVZ in the middle crust of Jiaodong gold province is the result of water-rock reaction alteration, but there are various possible sources of fluid genesis, including metamorphic fluids, meteoric water, and magmatic fluids. First, the fluid released during the metamorphism of Precambrian metamorphic rock (Jiaodong Group) is considered as a potential source and has been confirmed in greenstone or orogenic gold deposits in other ancient cratons in the world (Groves et al., 1998; Goldfarb et al., 2001). However, this possibility is the least likely for Jiaodong gold deposits, since the Precambrian metamorphism long predated the Mesozoic Au mineralization (Deng et al., 2014). Secondly, the participation of meteoric water is limited, as the depth of LVZ is generally greater than the circulation range of meteoric water in the upper crust (Whitmeyer and Wintsch, 2005). Even meteoric water can infiltrate deeply along the fault zone, but it is unlikely to form an alteration zone beneath the whole Jiaodong gold province. Therefore,

the most likely source of fluid is the Mesozoic magmas, including both granitic magma (such as Guojialing type granodiorite) and mantle-derived mafic magma (e.g., lamprophyre and diabase dikes in the ore field; Wang et al., 2022). The fluid released by these Mesozoic magmas may have accumulated in the weak zone of the middle crust, and fluid mixing and strong water-rock reaction occurred, forming the LVZ at the middle crust level. In Jiaodong gold province, the time consistency between the emplacement of Early Cretaceous granodiorite (~125 Ma) and mafic dikes (ca. 135–115 Ma), and regional gold mineralization (ca. 120–115 Ma), as well as the fluid geochemical data of gold deposits (Deng et al., 2020b, 2020c) all support above interpretation.

As mentioned earlier, the V_S perturbation image (Figure 6b) shows that there are two SE inclined velocity transitional zones below the SJZ and Qixia ore clusters, respectively, roughly corresponding to the Zhaoping fault and Qixia fault (Figure 6b), indicating that these faults may be connected to the underlying LVZ in a shovel-like manner. In addition, the lateral variations of velocity discontinuities below the junction of the Qixia and Muping ore clusters correspond well with the Wulian-Yantai and Muping fault on the surface (Figure 6b), which may indicate that the Wulian-Yantai fault cuts through the upper and middle crust in a nearly vertical manner. According to the close spatial relationship between these faults and gold deposits, we believe that these V_S images reveal the occurrence and structure characteristics of the deep part of the ore-controlling faults in Jiaodong gold province, that is, the overall characteristics of the metallogenic fluid migration network.

5.2.2 A potential source of Au

Like the source of ore-forming fluids, the gold source of the Jiaodong gold deposits is also controversial. Based on the intimacy of gold ores and mafic dikes, some geologists proposed that mafic magma probably provides part of metallogenic materials (Yang et al., 2003a; Tan et al., 2012; Cai et al., 2013; Ma et al., 2013; Deng et al., 2020b). On the other hand, zircon Hf isotopic mapping on the Mesozoic granitoids shows that most of the gold deposits are situated in a Neoproterozoic crustal domain, suggesting an old crustal source of gold (Deng et al., 2020c). Our V_S image provides new insights into plausible gold source.

The magma source for the ore-forming fluids in Jiaodong gold province also indicates that some of the gold was from mantle-derived magma or crust-derived magma. This has been confirmed by isotopic tracing studies on granite and ore deposits (Yang et al., 2003a; Ma et al., 2013; Deng et al., 2020b, 2020c). In addition, amphibolites in the high velocity body of the Jiaodong upper crust may be another source of gold. Previous studies have demonstrated that the protolith of amphibolites in the Jiaodong Group formed in an oceanic

subduction setting, rich in gold and other minerals (Hou et al., 2015, 2021). Although some gold and other ore-forming minerals may have experienced migration or loss during the Archean metamorphic process, a large amount of gold can still be extracted from them through later fluid circulation. From the perspective of spatial location, these amphibolites are located above the LVZ as high velocity bodies. When the ore fluid released from the LVZ migrated upward, it inevitably reacted with the amphibolite-rich crustal component and leached Au out of it by water-rock reaction, thus increasing the fertility of ore fluid. This water-rock reaction would be further intensified by the brittle fracturing of the upper crust during its extension and detachment. We, therefore, suggest that the amphibolites in the high velocity body could have contributed additional gold to the ore fluid (Figure 10).

5.2.3 Structural control on the style of gold mineralization

In the partitional deformation system in the upper and middle crustal levels, the styles of Au mineralization display regional differences. Our data show that the differences in ore-controlling faults and their geological environments are responsible for the spatial contrasts in mineralization styles.

The SJZ ore cluster is mainly controlled by a large-scale detachment fault system, as shown by our V_s image (Figure 6). The development of the LVZ could act as an important trigger for the development of subhorizontal detachment faults in the deep root of the listric fault system (Selverstone et al., 2012). This inference is partly evidenced by the convergence of the listric fault into LVZ at depth (Figure 6). This detachment system is dominated by permeable small cracks and pores, and the ore-forming fluid migrated along the gently dipping faults in the form of seepage flows. The intensive water-rock reaction and resultant sulfidation formed a large quantity of disseminated and veinlet-stockwork ores, leading to the formation of large-scale altered-rock type mineralization (Deng et al., 2020a). On the contrary, the Muping ore cluster is mainly controlled by high-angle brittle faults with high permeability. The ore-forming fluids migrated upward along the fault in the form of channel flows, and directly crystallized and precipitated into wider veins at suitable parts in the fracture zone, forming quartz-vein type mineralization with relatively small tonnage (Yang et al., 2014; Li et al., 2015; Song et al., 2015; Song, 2015). Like the SJZ, the Qixia ore cluster is also controlled by a detachment fault, but this cluster is dominantly underlain by metamorphic rocks without an amphibolite-rich layer, thus yielding less Au reserve. Moreover, a vertical dome and horizontal extension in the upper crust, as indicated by the uplifted LVZ (Figure 6b), led to more fractured channels and promoted the penetrability, thus resulting in the development of both quartz-vein and disseminated-veinlet mineralization types in this cluster.

5.3 A plausible metallogenic model for the Jiaodong gold province

This study reveals a new image of crustal architecture in the Jiaodong gold province, providing new constraints and insights into the genesis of gold mineralization. Based on the above discussion, we tentatively propose a new genetic model, addressing the sources of fluid and gold and the structural control on the styles of Au mineralization (Figure 10).

During the mineralization in the early Cretaceous (about 135–120 Ma), the partial melting of metasomatized mantle and the middle-lower crust, triggered by upwelling asthenosphere, led to the generation of the hydrous mafic and acidic magmas, respectively (Niu, 2005; Menzies et al., 2007; Zhu and Zheng, 2009; Zhu et al., 2015). These magmas released gold-bearing fluids and volatiles (H_2O , CO_2 , Cl) during their ascent, and these released phase, as well as the magmas themselves converged in the weak zone of the middle crust and reacted with surrounding rocks, leading to extensive and intensive alteration (LVZ). The ore fluids continuously migrated upwards and inevitably reacted with the upper-crustal amphibolites whose protolith has an arc origin and is rich in gold. These processes leached the gold into the fluid, thus increasing the fluid fertility. These gold-rich fluids were eventually transported to the shallow crust along different ore-controlling fault systems. In addition to continuous reactions with the surrounding rocks, due to the reduction of temperature and pressure or mixing with meteoric water, gold and other ore-forming minerals eventually precipitated to form gold ores. At the same time, due to the different occurrences, properties, and geological environments of ore-controlling faults, contrasting types of gold mineralization emerged as mentioned above.

6. Conclusions

(1) An intra-crustal LVZ at 12–20 km depth is imaged beneath the Jiaodong gold province. This LVZ, interpreted as a hydrothermal alteration zone, is considered to form due to water-rock reaction in the process of early Cretaceous magma accumulation, crystallization and degassing in the middle crust. Thus, the LVZ is interpreted to be a record of large-scale ore-forming fluid processes in the Jiaodong gold province.

(2) High velocity bodies at 8–12 km depth in the upper crust are identified beneath the SJZ ore cluster, which reflect abundant Neoproterozoic amphibolites in the upper crust. These amphibolites are usually high in Au content and likely provide extra gold into the ore fluid via leaching during the water-rock interaction, which explains the large metal tonnage in the western part of Jiaodong gold province.

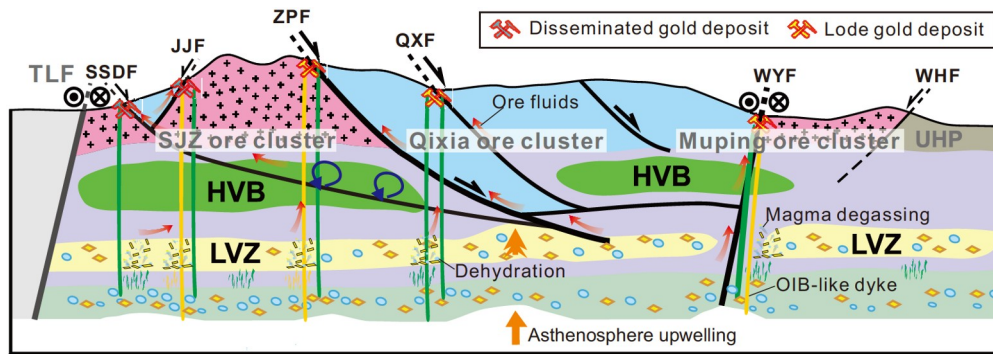


Figure 10 A schematic of metallogenic model of Jiaodong gold province. LVZ, low velocity zone; HVB, high velocity body; TLF, Tanlu fault; SSDF, Sanshandao fault; JJF, Jiaojia fault; ZPF, Zhaoping fault; QXF, Qixia fault; WYF, Wulian-Yantai fault; UHP, ultrahigh pressure metamorphic belt; WHF, Weihai fault.

(3) Our velocity image clearly reveals a gently inclined detachment system in the SJZ ore cluster and a steeply inclined fault system in the Muping ore cluster. We argue that such differences in the crustal architecture control regional preferences of mineralization styles in the Jiaodong province.

(4) Based on the velocity structure obtained from ambient seismic noise tomography and the existing geological data, a model of gold mineralization system is established, which can explain the origin of the ore-forming fluid and material sources, and the fault networks that control gold mineralization patterns.

Acknowledgements We would like to express our sincere appreciation and deep-felt memory to our former group leader and good friend, Prof. Zhongjie ZHANG, who suddenly passed away ten years ago (2013). We appreciate the assistance of the IGGCAS Seismic Array Laboratory and the members of the NCISP9 field team who collected data for this study, including Drs. Guiping YU, Enbo FAN, Guangli ZHANG, Haodong ZHANG, Fanchang MENG, Minfu HUANG and Fan ZHENG. We are grateful to Profs. Tianyu ZHENG, Laicheng MIAO, Jinhui YANG, Lin CHEN, and Wei LIN for the helpful discussion on the interpretation of our results. We thank the Data Management Center of the China National Seismic Network at the Institute of Geophysics, China Earthquake Administration (SEISDMC, doi: 10.7914/SN/CB), for providing seismic data from the permanent stations used. This study was financially supported by the Chinese National Key Research and Development Program (Grant Nos. 2019YFA0708602, 2016YFC0600101) and the National Natural Science Foundation of China (Grant No. 42130807).

Conflict of interest The authors declare that they have no conflict of interest.

References

- Ames L, Zhou G, Xiong B. 1996. Geochronology and isotopic character of ultrahigh-pressure metamorphism with implications for collision of the Sino-Korean and Yangtze cratons, central China. *Tectonics*, 15: 472–489
- Bensen G D, Ritzwoller M H, Barmin M P, Levshin A L, Lin F, Moschetti M P, Shapiro N M, Yang Y. 2007. Processing seismic ambient noise data to obtain reliable broad-band surface wave dispersion measurements. *Geophys J Int*, 169: 1239–1260
- Brocher T M. 2005. Empirical relations between elastic wave speeds and density in the Earth's crust. *Bull Seismol Soc Am*, 95: 2081–2092
- Cai Y C, Fan H R, Santosh M, Liu X, Hu F F, Yang K F, Lan T G, Yang Y H, Liu Y. 2013. Evolution of the lithospheric mantle beneath the southeastern North China Craton: Constraints from mafic dikes in the Jiaobei terrain. *Gondwana Res*, 24: 601–621
- Charles N, Augier R, Gumiaux C, Monié P, Chen Y, Faure M, Zhu R. 2013. Timing, duration and role of magmatism in wide rift systems: Insights from the Jiaodong Peninsula (China, East Asia). *Gondwana Res*, 24: 412–428
- Chen L, Zheng T, Xu W. 2006. A thinned lithospheric image of the Tanlu Fault Zone, eastern China: Constructed from wave equation based receiver function migration. *J Geophys Res*, 111: B09312
- Chough S K, Kwon S T, Ree J H, Choi D K. 2000. Tectonic and sedimentary evolution of the Korean peninsula: A review and new view. *Earth-Sci Rev*, 52: 175–235
- Christensen N I, Mooney W D. 1995. Seismic velocity structure and composition of the continental crust: A global view. *J Geophys Res*, 100: 9761–9788
- Deng J, Liu X, Wang Q, Pan R. 2014. Origin of the Jiaodong-type Xinli gold deposit, Jiaodong Peninsula, China: Constraints from fluid inclusion and C–D–O–S–Sr isotope compositions. *Ore Geol Rev*, 65: 674–686
- Deng J, Liu X, Wang Q, Dilek Y, Liang Y. 2017. Isotopic characterization and petrogenetic modeling of Early Cretaceous mafic dike—Lithospheric extension in the North China craton, eastern Asia. *GSA Bull*, 129: 1379–1407
- Deng J, Qiu K F, Wang Q F, Goldfarb R, Yang L Q, Zi J W, Geng J Z, Ma Y. 2020b. *In situ* dating of hydrothermal monazite and implications for the geodynamic controls on ore formation in the Jiaodong gold province, eastern China. *Econ Geol*, 115: 671–685
- Deng J, Wang Q. 2016. Gold mineralization in China: Metallogenic provinces, deposit types and tectonic framework. *Gondwana Res*, 36: 219–274
- Deng J, Wang Q, Santosh M, Liu X, Liang Y, Yang L, Zhao R, Yang L. 2020a. Remobilization of metasomatized mantle lithosphere: A new model for the Jiaodong gold province, eastern China. *Miner Depos*, 55: 257–274
- Deng J, Wang Q, Liu X, Zhang L, Yang L, Qiu K, Guo L, Liang Y, Ma Y. 2022. The Formation of the Jiaodong gold province. *Acta Geol Sin-Engl Ed*, 96: 1801–1820
- Deng J, Yang L Q, Groves D I, Zhang L, Qiu K F, Wang Q F. 2020c. An integrated mineral system model for the gold deposits of the giant Jiaodong province, eastern China. *Earth-Sci Rev*, 208: 103274
- Deng J, Wang Q F, Zhang L, Xue S C, Liu X F, Yang L, Yang L Q, Qiu K F, Liang Y Y. 2023. Metallogenic model of Jiaodong-type gold deposits, eastern China. *Sci China Earth Sci*, 66: 2287–2310
- Diaferia G, Cammarano F. 2017. Seismic signature of the continental crust:

- What thermodynamics says. An example from the Italian Peninsula. *Tectonics*, 36: 3192–3208
- Fan H R, Zhai M G, Xie Y H, Yang J H. 2003. Ore-forming fluids associated with granite-hosted gold mineralization at the Sanshandao deposit, Jiaodong gold province, China. *Miner Depos*, 38: 739–750
- Fang H, Yao H, Zhang H, Huang Y C, van der Hilst R D. 2015. Direct inversion of surface wave dispersion for three-dimensional shallow crustal structure based on ray tracing: Methodology and application. *Geophys J Int*, 201: 1251–1263
- Flinders A F, Shelly D R, Dawson P B, Hill D P, Tripoli B, Shen Y. 2018. Seismic evidence for significant melt beneath the Long Valley Caldera, California, USA. *Geology*, 46: 799–802
- Goldfarb R J, Groves D I, Gardoll S. 2001. Orogenic gold and geologic time: A global synthesis. *Ore Geol Rev*, 18: 1–75
- Goldfarb R J, Santosh M. 2014. The dilemma of the Jiaodong gold deposits: Are they unique? *Geosci Front*, 5: 139–153
- Goldfarb R J, Hart C, Davis G, Groves D. 2007. East Asian gold-deciphering the anomaly of Phanerozoic gold in Precambrian cratons. *Econ Geol*, 102: 341–345
- Goss S C, Wilde S A, Wu F, Yang J. 2010. The age, isotopic signature and significance of the youngest Mesozoic granitoids in the Jiaodong Terrane, Shandong Province, North China Craton. *Lithos*, 120: 309–326
- Groves D I, Goldfarb R J, Gebre-Mariam M, Hagemann S G, Robert F. 1998. Orogenic gold deposits: A proposed classification in the context of their crustal distribution and relationship to other gold deposit types. *Ore Geol Rev*, 13: 7–27
- Guo J H, Chen F K, Zhang X M, Siebel W, Zhai M G. 2005. Evolution of syn- to post-collisional magmatism from north Sulu UHP belt, eastern China: zircon U-Pb geochronology (in Chinese). *Acta Petrol Sin*, 21: 1281–1301
- Hacker B R, Ritzwoller M H, Xie J. 2014. Partially melted, mica-bearing crust in Central Tibet. *Tectonics*, 33: 1408–1424
- Henley R W, Berger B R. 2013. Nature's refineries—Metals and metalloids in arc volcanoes. *Earth-Sci Rev*, 125: 146–170
- Herrmann R B. 2013. Computer programs in seismology: An evolving tool for instruction and research. *Seismol Res Lett*, 84: 1081–1088
- Herrmann R B, Ammon C J. 2002. Computer programs in seismology: Surface waves, receiver functions and crustal structure, version 3.30. Saint Louis: Saint Louis University
- Hoggard M J, Czarnota K, Richards F D, Huston D L, Jaques A L, Ghelichkhan S. 2020. Global distribution of sediment-hosted metals controlled by craton edge stability. *Nat Geosci*, 13: 504–510
- Hou J, Wu C L, Yu G P, Xu T, Ai Y S. 2022. Research progress on the deep structure of Jiaodong gold deposit concentration area (in Chinese). *Prog Geophys*, 37: 952–963
- Hou Z Q, Xu B, Zheng Y C, Zheng H W, Zhang H R. 2021. Mantle flow: The deep mechanism of large-scale growth in Tibetan Plateau. *Chin Sci Bull*, 66: 2671–2690
- Hou Z Q, Duan L F, Lu Y J, Zheng Y C, Zhu D C, Yang Z M, Yang Z S, Wang B D, Pei Y R, Zhao Z D, McCuaig T C. 2015. Lithospheric architecture of the Lhasa terrane and its control on ore deposits in the Himalayan-Tibetan orogen. *Econ Geol*, 110: 1541–1575
- Hou Z Q, Pan X F, Yang Z M, Qu X F. 2007. Porphyry Cu-(Mo-Au) Deposits not Related to Oceanic-Slab Subduction: Examples from Chinese Porphyry Deposits in Continental Settings (in Chinese). *Geoscience*, 21: 332–351
- Huang J, Zheng Y F, Zhao Z F, Wu Y B, Zhou J B, Liu X. 2006. Melting of subducted continent: Element and isotopic evidence for a genetic relationship between Neoproterozoic and Mesozoic granitoids in the Sulu orogen. *Chem Geol*, 229: 227–256
- Jia S X, Wang F Y, Tian X F, Duan Y H, Zhang J S, Liu B F, Lin J Y. 2014. Crustal structure and tectonic study of North China Craton from a long deep seismic sounding profile. *Tectonophysics*, 627: 48–56
- Jiang G Z, Hu S B, Shi Y Z, Zhang C, Wang Z T, Hu D. 2019. Terrestrial heat flow of continental China: Updated dataset and tectonic implications. *Tectonophysics*, 753: 36–48
- Kozlovsky Y A. 1986. The Superdeep Well of the Kola Peninsula. Berlin: Springer Verlag
- Large S J E, Buret Y, Wotzlaw J F, Karakas O, Guillong M, von Quadt A, Heinrich C A. 2021. Copper-mineralised porphyries sample the evolution of a large-volume silicic magma reservoir from rapid assembly to solidification. *Earth Planet Sci Lett*, 563: 116877
- Li C, Chen C, Dong D, Kuponiyi A P, Dosso S E, Su D. 2018. Ambient noise tomography of the Shandong province and its implication for Cenozoic intraplate volcanism in eastern China. *Geochem Geophys Geosyst*, 19: 3286–3301
- Li L, Santosh M, Li S R. 2015. The 'Jiaodong type' gold deposits: Characteristics, origin and prospecting. *Ore Geol Rev*, 65: 589–611
- Liang Y, Deng J, Liu X, Wang Q, Qin C, Li Y, Yang Y, Zhou M, Jiang J. 2018. Major and trace element, and Sr isotope compositions of clinopyroxene phenocrysts in mafic dykes on Jiaodong Peninsula, southeastern North China Craton: Insights into magma mixing and source metasomatism. *Lithos*, 302-303: 480–495
- Liu C Z, Yin W Q, Zhang J, Zeng L H, Ouyang K G. 2009. Ore-controlling factors and prospecting prediction criteria of the Sn-Cu polymetallic deposit in Wuyishan metallogenic zone (in Chinese). *Miner Resour Geol*, 23: 124–128
- Liu L, Liu F, Liu P, Wang W, Ji L, Wang F, Cai J. 2018. Petrology, geochemistry and geochronology of the meta-mafic rocks in the North Sulu ultrahigh-pressure belt: Implications for their petrogenetic diversity and complex tectonic evolution. *Precambrian Res*, 316: 127–154
- Lin W, Wei W. 2018. Late Mesozoic extensional tectonics in the North China Craton and its adjacent regions: a review and synthesis. *Int Geol Rev*, 62: 811–839
- Ludwig W, Nafe J, Drake C. 1970. Seismic Refraction. In: Maxwell A E, ed. *The Sea: Ideas and Observations on Progress in the Study of the Sea*. New York-London-Sydney Toronto: Wiley Interscience, John Wiley & Sons
- Luo S, Yao H, Zhang Z, Bem T S. 2022. High-resolution crustal and upper mantle shear-wave velocity structure beneath the central-southern Tanlu fault: Implications for its initiation and evolution. *Earth Planet Sci Lett*, 595: 117763
- Luo Y, Yang Y, Xu Y, Xu H, Zhao K, Wang K. 2015. On the limitations of interstation distances in ambient noise tomography. *Geophys J Int*, 201: 652–661
- Ma L, Jiang S Y, Hou M L, Dai B Z, Jiang Y H, Yang T, Zhao K D, Pu W, Zhu Z Y, Xu B. 2013. Geochemistry of Early Cretaceous calc-alkaline lamprophyres in the Jiaodong Peninsula: Implication for lithospheric evolution of the eastern North China Craton. *Gondwana Res*, 25: 859–872
- Ma X Y, Liu C Q, Liu G D. 1991. Xiangshui (Jiangsu province) to Mandal (Nei Mon-GGOL) geoscience transect. *Acta Geol Sin*, 3: 199–215
- Marquis G, Hyndman R D. 1992. Geophysical support for aqueous fluids in the deep crust: Seismic and electrical relationships. *Geophys J Int*, 110: 91–105
- Martyn U. 2003. Studying continental dynamics with magnetotelluric exploration. *Earth Sci Front*, 10: 25–38
- Meng L, Lin W. 2021. Episodic crustal extension and contraction characterizing the Late Mesozoic tectonics of East China: Evidence from the Jiaodong Peninsula, East China. *Tectonics*, 40: E2020TC006318
- Meng Y F, Yao H J, Wang X Z. 2019. Crustal velocity structure and deformation features in the central-southern segment of Tanlu fault zone and its adjacent area from ambient noise tomography (in Chinese). *Chin J Geophys*, 62: 2490–2509
- Menzies M A, Xu Y G, Zhang H F, Fan H R. 2007. Integration of geology, geophysics and geochemistry: A key to understanding the North China Craton. *Lithos*, 96: 1–21
- Montagner J P, Nataf H C. 1986. A simple method for inverting the azimuthal anisotropy of surface waves. *J Geophys Res*, 91: 511–520
- Niu Y L. 2005. Generation and evolution of basaltic magmas: Some basic concepts and a hypothesis for the origin of the Mesozoic-Cenozoic volcanism in eastern China. *Geol J China Univ*, 11: 9–46
- Pan S Z, Wang F Y, Zheng Y P. 2015. Crustal velocity structure beneath Jiaodong Peninsula and its tectonic implications (in Chinese). *Chin J*

- Geophys, 58: 3251–3263
- Selverstone J, Axen G J, Luther A. 2012. Fault localization controlled by fluid infiltration into mylonites: Formation and strength of low-angle normal faults in the midcrustal brittle-plastic transition. *J Geophys Res*, 117: B06210
- Shan X, Zhai M G, Oliveira E P, Santosh M, Wang F. 2015. Convergent margin magmatism and crustal evolution during Archean-Proterozoic transition in the Jiaobei terrane: Zircon U-Pb ages, geochemistry, and Nd isotopes of amphibolites and associated grey gneisses in the Jiaodong complex, North China Craton. *Precambrian Res*, 264: 98–118
- Shearer P M. 2009. Introduction to Seismology. Cambridge: Cambridge University Press
- Sleep N H, Blanpied M L. 1994. Ductile creep and compaction: A mechanism for transiently increasing fluid pressure in mostly sealed fault zones. *Pure Appl Geophys*, 143: 9–40
- Song M C. 2015. The main achievements and key theory and methods of deep-seated prospecting in the Jiaodong gold concentration area, Shandong Province. *Geol Bull China*, 34: 1758–1771
- Song M, Li S, Santosh M, Zhao S, Yu S, Yi P, Cui S, Lv G, Xu J, Song Y, Zhou M. 2015. Types, characteristics and metallogenesis of gold deposits in the Jiaodong Peninsula, Eastern North China Craton. *Ore Geol Rev*, 65: 612–625
- Su D L, Fan J K, Wu S G, Chen C X, Dong X N, Chen S J. 2016. 3D P-wave velocity structures of crust and their relationship with earthquakes in the Shandong area (in Chinese). *Chin J Geophys*, 59: 1335–1349
- Tam P Y, Zhao G, Liu F, Zhou X, Sun M, Li S. 2011. Timing of metamorphism in the Paleoproterozoic Jiao-Liao-Ji Belt: New SHRIMP U-Pb zircon dating of granulites, gneisses and marbles of the Jiaobei massif in the North China Craton. *Gondwana Res*, 19: 150–162
- Tan J, Wei J, Audétat A, Pettker T. 2012. Source of metals in the Guocheng gold deposit, Jiaodong Peninsula, North China Craton: Link to early Cretaceous mafic magmatism originating from Paleoproterozoic metasomatized lithospheric mantle. *Ore Geol Rev*, 48: 70–87
- Tang J, Zheng Y F, Wu Y B, Gong B, Zha X, Liu X. 2008. Zircon U-Pb age and geochemical constraints on the tectonic affinity of the Jiaodong terrane in the Sulu orogen, China. *Precambrian Res*, 161: 389–418
- Tarantola A, Valette B. 1982. Generalized nonlinear inverse problems solved using the least squares criterion. *Rev Geophys*, 20: 219–232
- Wan Y, Liu D, Dong C, Liu S, Wang S, Yang E. 2011. U-Th-Pb behavior of zircons under high-grade metamorphic conditions: A case study of zircon dating of meta-diorite near Qixia, eastern Shandong. *Geosci Front*, 2: 137–146
- Wang J, Chang S C, Lu H B, Zhang H C. 2016. Detrital zircon provenance of the Wangshi and Laiyang groups of the Jiaolai basin: Evidence for Early Cretaceous uplift of the Sulu orogen, Eastern China. *Int Geol Rev*, 58: 719–736
- Wang Q F, Yang L, Zhao H S, Groves D I, Weng W J, Xue S C, Li H J, Dong C Y, Yagn L Q, Li D P, Deng J. 2022. Towards a universal model for orogenic gold systems: A perspective based on Chinese examples with geodynamic, temporal, and deposit-scale structural and geochemical diversity. *Earth-Sci Rev*, 224: 103861
- Wang Q F, Zhao H S, Groves D I, Deng J, Zhang Q W, Xue S C. 2020. The Jurassic Danba hypozonal orogenic gold deposit, western China: Indirect derivation from fertile mantle lithosphere metasomatized during Neoproterozoic subduction. *Miner Depos*, 55: 309–324
- Whitmeyer S J, Wintsch R P. 2005. Reaction localization and softening of texturally hardened mylonites in a reactivated fault zone, central Argentina. *J Metamorph Geol*, 23: 411–424
- Xu B, Hou Z Q, Griffin W L, Zheng Y, Wang T, O'Reilly S Y. 2021. Cenozoic lithospheric architecture and metallogenesis in southeastern Tibet. *Earth-Sci Rev*, 214: 1–26
- Xu P, Liu F, Ye K, Wang Q, Cong B, Chen H. 2002. Flake tectonics in the Sulu orogen in eastern China as revealed by seismic tomography. *Geophys Res Lett*, 29: 23-1–23-4
- Xu Y, Li Z W, Kim K, Hao T Y, Liu J S. 2009. Crustal velocity structure and collision boundary between the Sino-Korea and Yangtze blocks in the Yellow Sea (in Chinese). *Chin J Geophys*, 52: 646–652
- Yang J H, Chu M F, Liu W, Zhai M G. 2003b. Geochemistry and petrogenesis of Guojialing granodiorites from the northwestern Jiaodong Peninsula, eastern China. *Acta Petrol Sin*, 19: 692–700
- Yang J H, Wu F Y, Wilde S A. 2003a. A review of the geodynamic setting of large-scale Late Mesozoic gold mineralization in the North China Craton: an association with lithospheric thinning. *Ore Geol Rev*, 23: 125–152
- Yang L Q, Deng J, Wang Z L. 2014. Mesozoic gold metallogenic system of the Jiaodong gold province, eastern China. *Acta Petrol Sin*, 30: 2247–2467
- Yang L, Zhao R, Wang Q, Liu X, Carranza E J M. 2018. Fault geometry and fluid-rock reaction: Combined controls on mineralization in the Xinli gold deposit, Jiaodong Peninsula, China. *J Struct Geol*, 111: 14–26
- Yang W. 2002. Geophysical profiling across the Sulu ultra-high-pressure metamorphic belt, eastern China. *Tectonophysics*, 354: 277–288
- Yang Y, Ritzwoller M H, Levshin A L, Shapiro N M. 2007. Ambient noise Rayleigh wave tomography across Europe. *Geophys J Int*, 168: 259–274
- Yang Y J, Ritzwoller M H, Zheng Y, Shen W S, Levshin A L, Xie Z J. 2012. A synoptic view of the distribution and connectivity of the mid-crustal low velocity zone beneath Tibet. *J Geophys Res*, 117: B04303
- Yao H J, Gouépard P, Collins J A, McGuire J J, van der Hilst R D. 2011. Structure of young East Pacific Rise lithosphere from ambient noise correlation analysis of fundamental- and higher-mode Scholte-Rayleigh waves. *Comptes Rendus Geosci*, 343: 571–583
- Yao H J, van der Hilst R D, de Hoop M V. 2006. Surface-wave array tomography in SE Tibet from ambient seismic noise and two-station analysis—I. Phase velocity maps. *Geophys J Int*, 166: 732–744
- Yao H J, van der Hilst R D, Montagner J P. 2010. Heterogeneity and anisotropy of the lithosphere of SE Tibet from surface wave array tomography. *J Geophys Res*, 115: B12307
- Yu G P, Xu T, Ai Y S, Chen L, Yang J H. 2020b. Significance of crustal extension and magmatism to gold deposits beneath Jiaodong Peninsula, eastern North China Craton: Seismic evidence from receiver function imaging with a dense array. *Tectonophysics*, 789: 228532
- Yu G P, Xu T, Liu J T, Ai Y S. 2020a. Late Mesozoic extensional structures and gold mineralization in Jiaodong Peninsula, eastern North China Craton: An inspiration from ambient noise tomography on data from a dense seismic array (in Chinese). *Chin J Geophys*, 63: 1878–1893
- Yu N, Wang E, Wang X, Kong W, Li D, Li R. 2022. The influence of the Ailaoshan-Red River shear zone on the mineralization of the Beiya deposit on the southeastern margin of the Tibetan Plateau revealed by a 3-D magnetotelluric survey. *J Geophys Res-Solid Earth*, 127: E2021JB022923
- Yu X, Shan W, Xiong Y, Geng K, Sun Y, Chi N, Guo B, Li D, Li H, Song Y, Yang D. 2018. Deep structural framework and genetic analysis of gold concentration areas in the northwestern Jiaodong Peninsula, China: A new understanding based on high-resolution reflective seismic survey. *Acta Geol Sin-Engl Ed*, 92: 1823–1840
- Zhang K, Lü Q, Yan J, Hu H, Fu G M, Shao L. 2018. Crustal structure beneath the Jiaodong Peninsula, North China, revealed with a 3D inversion model of magnetotelluric data. *J Geophys Eng*, 15: 2442–2454
- Zhang M H, Wu Z B, Ma L X, Zheng F, Xie T T, Zheng M J, Hou J, Liu Y S, Zhang Y Q, Xu T, Bai Z M. 2020. Research progress of passive source detection technology based on short-period dense seismic array (in Chinese). *Progr Geophys*, 35: 495–511
- Zhang Y Q, Li J L, Zhang T. 2007. Late Mesozoic kinematic history of the Muping-Jimo fault zone in Jiaodong Peninsula, Shandong Province, East China. *Geol Rev*, 53: 289–300
- Zhang Y Q, Dong S W, Li J H, Cui J J, Shi W, Su J B, Li Y. 2012. The New Progress in the Study of Mesozoic Tectonics of South China (in Chinese). *Acta Geosci Sin*, 33: 257–279
- Zhao R, Wang Q, Liu X, Santosh M, Yuan W, Wang W. 2018. Uplift history of the Jiaodong Peninsula, eastern North China Craton: Implications for lithosphere thinning and gold mineralization. *Geol Mag*, 155: 979–991

- Zhao R, Wang Q F, Liu X F, Wang W, Pan R G. 2016. Architecture of the Sulu crustal suture between the North China Craton and Yangtze Craton: Constraints from Mesozoic granitoids. *Lithos*, 266-267: 348–361
- Zhao Z, Zhao Z X, Xu J R. 2012. Velocity structure heterogeneity and tectonic motion in and around the Tan-Lu fault of China. *J Asian Earth Sci*, 57: 6–14
- Zheng T Y, Zhao L, Xu W W, Zhu R X. 2008. Insight into modification of North China Craton from seismological study in the Shandong Province. *Geophys Res Lett*, 35: L22305
- Zhu R X, Chen L, Wu F Y, Liu J L. 2011. Timing, scale and mechanism of the destruction of the North China Craton. *Sci China Earth Sci*, 54: 789–797
- Zhu R X, Fan H R, Li J W, Meng Q R, Li S R, Zeng Q D. 2015. Decratonic gold deposits. *Sci China Earth Sci*, 58: 1523–1537
- Zhu R X, Zheng T Y. 2009. Destruction geodynamics of the North China craton and its Paleoproterozoic plate tectonics. *Sci Bull*, 54: 3354–3366

(Editorial handling: Huajian YAO)